Perfectly conducting incompressible fluid model of a wire array implosion

Alexander L. Velikovich
Plasma Physics Division, Naval Research Laboratory, Washington, DC 20375

Igor V. Sokolov
University of Michigan, Ann Arbor, Michigan 48109

Andrey A. Esaulov
Toyama University, Toyama 930-8555, Japan
and Institute of Theoretical and Experimental Physics, Moscow 117259, Russia

(Received 10 October 2001; accepted 19 December 2001)

An incompressible perfectly conducting magnetohydrodynamic model is applied to describe a multiwire array implosion on the (r,θ) plane using the theory of analytic functions. The plasma columns emerging from the electrical explosion of individual wires move and change the shape of their cross section in the magnetic field produced by the currents flowing on the surfaces of the columns and closing through a cylindrical return current can. Geometry of both the ''global'' and ''private'' magnetic fields and self-consistent distributions of the electric currents on the conducting surfaces are determined for any wire array configuration including nested wire arrays, wires close to the return current can, etc. The coupled equations of motion and magnetostatics for an essentially two-dimensional problem are reduced to one-dimensional parametric governing equations, written for the boundary of the fluid contours. The implosion dynamics is shown to be driven by a competition between the implosion pressure, making the array converge to the axis as a set of individual plasma columns, and the tidal pressure that makes the wires merge, forming an annular conducting shell. Their relative roles are determined by the gap-to-diameter ratio $\pi R_c(t)/NR_w(t)$. If this ratio is large at early time, then the array implodes as a set of individual plasma columns. Otherwise, when the ratio is about π or less, the tidal forces prevail, and the plasma columns tend to form a shell-like configuration before they start converging to the axis of the array. The model does not allow the precursor plasma streams to be ejected from the wires to the axis, indicating that this process is governed by the finite plasma conductivity and could only be described with a proper conductivity model. [DOI: 10.1063/1.1452104]

I. INTRODUCTION

The achievements of high current Z-pinch physics in recent years have been spectacular. Record values of total x-ray energy output ~2 MJ, peak total power >250 TW, argon (3.3 keV), and titanium (4.8 keV) *K*-shell yields over 270 and 125 kJ, respectively, have been produced on the 20 MA ''Z'' facility at Sandia National Laboratories.[1–3] To maximize the radiative performance of ''Z'' and other multi-MA current drivers, a careful design of the radiating loads is required. The actual Z-pinch plasma radiation sources (PRS) load designs used to obtain record-high yield and power emerged from a sustained effort of improving radiative properties of PRS through mitigating the Rayleigh–Taylor (RT) instability of implosion. The RT instability mitigation increases the radial compression of the pinch, and thereby the density of the radiating plasma, enhances the driver energy deposition to the plasma. The development of the gas-puff loads has progressed from annular puffs to uniform fills to the section of a gas jet produced by a recessed double-shell nozzle[3,4] that combines the features of double shells and tailored density profiles.[5,6] The wire array load design advanced through a significant increase in the number of wires in a cylindrical array,[7] and the use[1] of nested instead of single wire arrays.[8,9]

To advance further in the wire array load design, a better understanding of the implosion physics is needed. Being essentially a three-dimensional (3D) process,[10] a wire array implosion at the moment cannot be modeled numerically without sacrificing much of the relevant physics. Simplified two-dimensional (2D) models permit more detailed numerical and analytical investigation. The 2D (r,z) magnetohydrodynamic (MHD) modeling is fairly advanced,[5,11,12] and capable of capturing many essential features of the implosions, including the growth of the fastest $m=0$ RT and MHD instability modes and enhanced energy coupling to the pinch plasma.[11,13] However, since a wire array load is not an annular plasma shell, at least initially,[14] there are some important phenomena affecting the radiative performance, which cannot be described by the 2D (r,z) modeling. The most important of them are formation of the imploding plasma shell from the individual wire plasmas, ejection of the precursor plasma streams that converge to the axis prior to the implosion of the main plasma mass[15] and current splitting and/or switching between the components of the load in the nested wire arrays (including the case when it operates in the ''transparent inner'' mode)[8,9,16] or in hybrid loads like gas-puff-on-wire-array.[17] These 2D effects have to be modeled on the (r,θ) plane.

The 2D (r,θ) MHD modeling is possible (see Refs. 10, 14–16 and references therein) but still quite complicated. It is not certain yet how well the 2D MHD can reproduce some essential features of implosions, such as collisions between plasma layers, reconnection of magnetic field and switching of current between components of a nested load. This is why simplified approaches could be helpful, like the simple wire-dynamic model[8,9] used to study the implosion kinematics and current switching in nested wire array loads. The magnetostatic effects due to finite sizes of the wire plasmas are beyond the thin-wire approximation used in Refs. 8 and 9 and could only be treated numerically.[18]

Our present study extends the results of Refs. 8, 9, and 18. We investigate the (r,θ) dynamics of finite-size perfectly conducting plasma columns in a periodic array. Distribution of current density on the surfaces of the plasma columns and on the return current can, as well as the magnetic field in vacuum, are calculated self-consistently with the time-dependent cross-sectional shapes of the columns. This approach could be regarded as an alternative to the direct numerical integration of the MHD equations. Numerically, it is quite economical and has an attractive capacity of treating a plasma-vacuum boundary explicitly. Using the theory of analytic functions, one can describe 2D plasma dynamics in the global magnetic field of the wire array by integrating one-dimensional (1D) equations that refer to the field and plasma parameters on the surface of a plasma column. Thus we obtain a virtually exact solution, which provides a better insight into the physics of our simplified model. A similar analytical method has been applied in Ref. 19 to study nonlinear dynamics of the free surface of an ideal fluid.

This paper is structured as follows. In Sec. II we derive the equations that self-consistently describe the shape and motion of perfectly conducting incompressible fluid columns on the (x,y)—same as (r,θ)—plane. Section III presents the derivation of magnetic field and current distributions and formulas for self- and mutual inductance for plasma columns arranged as in a single or nested wire array inside a cylindrical return current can. Dynamics of wire array implosions described by this model is investigated numerically in Sec. IV. In Sec. V, we conclude with a discussion.

II. PLASMA DYNAMICS

A. Formulation of the problem

Consider a two-dimensional—(x,y) or (r,θ)—motion of the wire plasmas during an implosion of a periodic N-wire array. The wire plasma is modeled as a perfectly conducting, incompressible, irrotational, inviscid fluid. Physically, the assumption of perfect conductivity means that the current is concentrated in a thin skin layer on the plasma surface. This is not typical for high-current implosions, where the thickness of an imploding shell or individual wire is of the order of its skin depth, the magnetic Reynolds number being of order unity rather than very large, as required by the perfect conductivity assumption. The incompressibility assumption is not realistic either. Indeed, the plasma temperature during the run-in phase for most wire materials is controlled by radiation losses, and therefore the actual plasma density has to increase roughly as the magnetic pressure driving its implosion. Our plasma model is admittedly highly idealized and not directly applicable to the experimental conditions. The idealization of the problem, however, permits us to study it analytically, highlighting certain physics issues relevant in the general case, as well as generating virtually exact solutions, which could be used, in appropriate parameter ranges, to benchmark the hydrocodes. It should be added that our results pertaining to magnetostatics (current splitting between the components of a nested wire array, distribution of the return current on the surface of a cylindrical can, etc.) are not sensitive to the distributions of current and mass in individual wires. The corresponding formulas are therefore applicable whenever the impedance of the wire array load is mainly inductive, see below.

Initially, the wires are cylindrical columns equidistantly distributed over a circle whose radius is $R_c(0)$. The initial rotational symmetry of the Nth order, as well as the translational symmetry with respect to the displacements along the z axis, are supposed to be conserved during the implosion.

Denote the projection of the nth plasma column onto the complex plane $z=x+iy$ at the moment t by $\Re_n(t)$ with its boundary $\gamma_n(t)$. Due to the rotational symmetry of the system, one can write, omitting the subscript 1 for the first plasma column,

$$\gamma_n(t)=\gamma(t)\exp[2\pi i(n-1)/N]. \tag{1}$$

The Riemann theorem[20] states that while $\Re(t)$ remains a simply connected domain, for any instant t there exists a conformal mapping $z=\Xi(z_0,t)$ of the interior of the unit circle, $|z_0|\leqslant 1$ on the complex plane $z_0=x_0+iy_0$ onto the interior of the domain $\Re(t)$. The complex function $\Xi(z_0,t)$, as well as all its derivatives with respect to both arguments, z_0 and t, is analytic [moreover, $\partial\Xi(z_0,t)/\partial z_0\equiv\Xi_{z_0}\neq 0$] in the interior of the unit circle. This conformal mapping is determined by three parameters. Since the boundary of the unit circle $\exp(iu)$, $0\leqslant u\leqslant 2\pi$, is mapped to the boundary contour, $\gamma(t)$, we can introduce a complex function of a real argument u that also defines the boundary of the domain $\Re(t)$:

$$\gamma(t)=\Xi(e^{iu},t)=\xi(u,t)=\varsigma(u,t)+i\lambda(u,t). \tag{2}$$

If the real axis x is the axis of symmetry of the domain $\Re(0)$ at the initial moment, this mirror symmetry will be conserved at later time t due to the global rotational symmetry of the system. So one can assume that the points of the unit circle that belong to the real axis x_0 will be transformed by the conformal mapping Ξ to the points of the domain $\Re(t)$ on the real axis x: At any moment t,

$$\mathrm{Im}[z=\Xi(z_0,t)]=0 \quad \text{if } \mathrm{Im}(z_0)=0. \tag{3}$$

Thus we can fix two arbitrary parameters of the conformal mapping $z=\Xi(z_0,t)$ by eliminating an arbitrary rotation with respect to the center of the unit circle $z_0=0$:

$$\lambda(0,t)=0 \qquad \text{and} \quad \lambda(\pi,t)=0. \tag{4}$$

Schwartz integral[20] recovers the value of an analytic function $\Xi(z_0,t)$ in the interior of the domain $\Re(t)$ from the real part of its boundary value, $\varsigma(u,t)$:

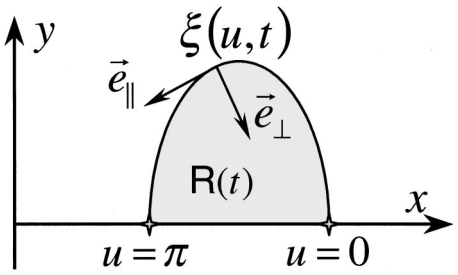

FIG. 1. The reference frame tied to the contour $\xi(u,t)$.

$$\Xi(z_0,t)=\frac{1}{2\pi}\int_0^{2\pi}\varsigma(u,t)\frac{e^{iu}+z_0}{e^{iu}-z_0}du+iC, \tag{5}$$

where C is an arbitrary real constant. From Eqs. (2) and (5) the imaginary part of the complex function $\xi(u,t)$ can be expressed via its real part in terms of an integral operator $\hat{H}$,

$$\lambda(u,t)=\hat{H}\varsigma(u,t)=\int_0^{2\pi}\varsigma(w,t)\cot\left(\frac{u-w}{2}\right)dw+C. \tag{6}$$

The time derivative of the function $\xi(u,t)$ is the boundary value of another analytic function, $\Xi_t\equiv\partial\Xi(z_0,t)/\partial t$,

$$\frac{\partial}{\partial t}\xi(u,t)\equiv\xi_t=\Xi_t(e^{iu},t)=V(u,t), \tag{7}$$

where $V(u,t)$ is the complex velocity of the point of the boundary contour with coordinate u. This complex vector can be expressed through its real components, $V_{||}$ and $V_\perp$,

$$V(u,t)=\mathbf{e}_{||}V_{||}(u,t)+\mathbf{e}_\perp V_\perp(u,t). \tag{8}$$

Here, $\mathbf{e}_{||}$ and $\mathbf{e}_\perp$ are complex unit vectors, and the frame of reference is tied to the contour $\xi(u,t)$, see Fig. 1,

$$\mathbf{e}_{||}=\frac{\xi_u}{|\xi_u|},\quad \mathbf{e}_\perp=i\frac{\xi_u}{|\xi_u|},\quad \xi_u\equiv\frac{\partial}{\partial u}\xi(u,t). \tag{9}$$

The components of the complex velocity are readily expressed via ξ and its derivatives

$$V_{||}(u,t)=\mathrm{Re}(\xi_t\overline{\mathbf{e}_{||}})=|\xi_u|\mathrm{Re}(\xi_t/\xi_u), \tag{10}$$

$$V_\perp(u,t)=\mathrm{Re}(\xi_t\overline{\mathbf{e}_\perp})=-|\xi_u|\mathrm{Re}(i\xi_t/\xi_u). \tag{11}$$

In Eqs. (10)–(11) and below, the bar denotes a complex conjugate value, $\overline{z}=x-iy$.

On the complex plane $z=x+iy$ a potential flow of an incompressible fluid in the domain $z\in\Re(t)$ is described by two real functions of complex argument; the velocity potential $\Phi(z,t)$ and the stream function $\Theta(z,t)$,

$$v_x=\frac{\partial\Phi}{\partial x}=\frac{\partial\Theta}{\partial y},\quad v_y=\frac{\partial\Phi}{\partial y}=-\frac{\partial\Theta}{\partial x}, \tag{12}$$

where v_x and v_y are, respectively, real and imaginary part of the complex velocity of the fluid, $v=v_x+iv_y$. The fluid is incompressible ($\nabla\cdot\mathbf{v}=0$) and irrotational ($\nabla\times\mathbf{v}=0$), which implies that both functions satisfy the Laplace equation

$$\nabla^2\Phi=0,\quad \nabla^2\Theta=0. \tag{13}$$

Defining the complex velocity potential as

$$X(z,t)=\Phi(z,t)+i\Theta(z,t), \tag{14}$$

we find that Eqs. (12) are the Cauchy–Riemann conditions which ensure that the complex function $X(z,t)$ and all its derivatives with respect to both arguments are analytic functions in the domain $\Re(t)$.

The velocity potential $\Phi(z,t)$ at the boundary of the domain $\Re(t)$ could be expressed as a function of the coordinate u and time,

$$\Phi(\xi(u,t),t)=\Psi(u,t). \tag{15}$$

This equation is generalized for the complex velocity potential in terms of the integral operator $\hat{H}$ introduced in Eq. (6),

$$X(\xi(u,t),t)=(1+i\hat{H})\Psi(u,t). \tag{16}$$

The analytic function $\partial X/\partial z$ and the complex velocity of the fluid are complex conjugate functions in $\Re(t)$,

$$\frac{\partial}{\partial z}X(z,t)=\overline{v}(z,t),\quad z\in\Re(t). \tag{17}$$

Thus $v(z,t)$ is an antianalytic function in $\Re(t)$, its real and imaginary parts satisfying the Cauchy–Riemann conditions with inverted signs [e.g., compared to (12)]. The boundary value of the analytic function $\overline{v}(z,t)$ at the point u is

$$\overline{v}(\xi(u,t),t)=\left.\frac{\partial X}{\partial z}\right|_{z=\xi}=\frac{1}{\xi_u}(1+i\hat{H})\Psi_u(u,t), \tag{18}$$

because the integral operator $\hat{H}$ is commutative with the differential operator $\partial/\partial u$,

$$\frac{\partial}{\partial u}\hat{H}\Psi(u,t)=\hat{H}\frac{\partial}{\partial u}\Psi(u,t)\equiv\hat{H}\Psi_u. \tag{19}$$

With the aid of Eq. (9) we express the boundary value of the fluid velocity via its real components $v_{||}$ and $v_\perp$ as

$$v(\xi(u,t),t)=\mathbf{e}_{||}v_{||}(u,t)+\mathbf{e}_\perp v_\perp(u,t), \tag{20}$$

where the longitudinal component $v_{||}(u,t)$ equals

$$v_{||}(u,t)=\mathrm{Re}(\mathbf{e}_{||}\overline{v}(\xi,t))=\mathrm{Re}\left(\frac{\xi_u}{|\xi_u|}\left.\frac{\partial X}{\partial z}\right|_{z=\xi}\right)=\frac{\Psi_u}{|\xi_u|}, \tag{21}$$

and the normal component $v_\perp(u,t)$ equals

$$v_\perp(u,t)=\mathrm{Re}(\mathbf{e}_\perp\overline{v}(\xi,t))=-\frac{\hat{H}\Psi_u}{|\xi_u|}. \tag{22}$$

B. Equation of motion for the fluid contour

In Sec. II A, two complex functions have been introduced at the point of the boundary contour ξ with coordinate u: the velocity of motion of this point, $V(u,t)$, and the fluid velocity at this point, $v(\xi(u,t),t)$. Generally, they are not equal to each other, $V(u,t)\neq v(\xi(u,t))$. Indeed, the first function characterizes the conformal mapping $\Xi(z_0,t)$, and the second one is the physical velocity. Moreover, $V(u,t)$ is the boundary value of an analytic function Ξ_t, whereas the function $v(z,t)$ is antianalytic in $\Re(t)$. Nevertheless, in the reference frame (9) tied to the contour ξ, the normal compo-

nents of these two velocities are the same, $v_\perp(u,t) = V_\perp(u,t)$. Therefore, the equation of motion for the contour follows from (11) and (22):

$$\mathrm{Re}\left(\frac{i\xi_t}{\xi_u}\right) = \frac{\hat{H}\Psi_u}{|\xi_u|^2}. \tag{23}$$

The left-hand side of Eq. (23) is the real part of the boundary value of a function $g(z_0,t)$, which is defined in the interior of the unit circle, $|z_0| \leqslant 1$,

$$\frac{i\xi_t(u,t)}{\xi_u(u,t)} = g(z_0,t)|_{z_0=\exp(iu)}. \tag{24}$$

Since $\xi(u,t)$ is the boundary value of $\Xi(z_0,t)$ on the unit circle $z_0 = e^{iu}$, the following relations hold:

$$\xi_t(u,t) = \Xi_t(z_0,t)|_{z_0=\exp(iu)}, \tag{25}$$

$$\xi_u(u,t) = \left(\frac{\partial z_0}{\partial u}\frac{\partial \Xi}{\partial z_0}\right)_{z_0=\exp(iu)} = (iz_0\Xi_{z_0})_{z_0=\exp(iu)}. \tag{26}$$

In Eq. (26) the dependence $z_0(u) = e^{iu}$, initially defined on the unit circle boundary $|z_0| = 1$, was analytically continued in the interior of the unit circle, so that $z_0 = |z_0|e^{iu}$, and $\partial z_0/\partial u = iz_0$ for $|z_0| \leqslant 1$. Thus we have

$$g(z_0,t) = \frac{1}{z_0} \times \frac{\Xi_t(z_0,t)}{\Xi_{z_0}(z_0,t)}, \quad |z_0| \leqslant 1. \tag{27}$$

Obviously, $g(z_0,t)$ is not an analytic function in the interior of the unit circle, since it has a pole $\sim 1/z_0$ at the point $z_0 = 0$ (note that $\Xi_{z_0} \neq 0$ for $|z_0| \leqslant 1$). However, one can construct an auxiliary function $G(z_0,t)$ that is analytic in the unit circle

$$G(z_0,t) = g - \frac{1}{z_0} \times \lim_{z_0 \to 0}(z_0 g) = g(z_0,t) - \frac{F(t)}{z_0}, \tag{28}$$

where

$$F(t) = \frac{\Xi_t(z_0,t)|_{z_0=0}}{\Xi_{z_0}(z_0,t)|_{z_0=0}} \tag{29}$$

is a real-valued function, see below. Substituting $g(e^{iu},t)$ expressed via $G(e^{iu},t)$ into Eq. (23), we obtain

$$\mathrm{Re}\left(i\frac{\xi_t}{\xi_u} - F(t)e^{-iu}\right) = \frac{\hat{H}\Psi_u}{|\xi_u|^2} - F(t)\cos u. \tag{30}$$

Since the function $G(z_0,t)$ is analytic in the interior of the unit circle $|z_0| \leqslant 1$, the imaginary part of its boundary value can be recovered from its real part by applying the integral operator $\hat{H}$ to both sides of Eq. (30),

$$\mathrm{Im}\left(i\frac{\xi_t}{\xi_u} - F(t)e^{-iu}\right) = \hat{H}\frac{\hat{H}\Psi_u}{|\xi_u|^2} - F(t)\sin u. \tag{31}$$

Summing Eqs. (30) and (31), we obtain the equation for the evolution of the function $\xi(u,t)$,

$$V(u,t) = \xi_t = \xi_u\left[(\hat{H} - i)\frac{\hat{H}\Psi_u}{|\xi_u|^2} - 2F(t)\sin u\right]. \tag{32}$$

From Eq. (10), we find the longitudinal component of the velocity of the point with coordinate u on the boundary contour $\xi(u,t)$,

$$V_{||} = |\xi_u|\left[\hat{H}\frac{\hat{H}\Psi_u}{|\xi_u|^2} - 2F(t)\sin u\right]. \tag{33}$$

The denominator of the right-hand side of Eq. (29) is a function of time

$$\Xi_{z_0}(z_0,t)|_{z_0=0} = f(t). \tag{34}$$

This function could be found by integrating the function $\Xi_{z_0}(z_0,t)$, which is analytic in the circle $|z_0| \leqslant 1$, over the contour $z_0 = e^{iu}$, using the mean-value theorem

$$f(t) = \frac{1}{2\pi}\int_0^{2\pi}(\Xi_{z_0})_{z_0=\exp(iu)}du = \frac{1}{2\pi i}\int_0^{2\pi}\xi_u e^{-iu}\,du. \tag{35}$$

If the contour $\xi(u,t)$ is symmetrical with respect to the real axis x, then

$$f(t) = \frac{1}{2\pi}\int_0^{2\pi}[(\hat{H}\mathfrak{s}_u)\cos u - \mathfrak{s}_u \sin u]du. \tag{36}$$

The numerator of the right-hand side of Eq. (29) is the velocity $V_c(t)$ of the point $z_c(t) = \Xi(0,t)$ representing the image of the center of the unit circle,

$$\Xi_t(z_0,t_0)|_{z_0=0} = \frac{d}{dt}z_c(t) = V_c(t). \tag{37}$$

According to Eq. (4), the easiest way to define the position of the point z_c is the following:

$$z_c(t) = \tfrac{1}{2}[\mathfrak{s}(0,t) + \mathfrak{s}(\pi,t)]. \tag{38}$$

Equation (38) ensures that the point z_c always remains within the domain $\mathfrak{R}(t)$, as long as it remains simply connected. Postulating (38), we fix the last free parameter of the conformal mapping $z = \Xi(z_0,t)$ [the other two have been fixed by Eq. (4)]. The velocity $V_c(t)$ is found from Eq. (38),

$$V_c(t) = \tfrac{1}{2}[\mathfrak{s}_t(0,t) + \mathfrak{s}_t(\pi,t)]. \tag{39}$$

For example, for a uniform distribution of the fluid velocity, $v(z,t) = v_0$, where v_0 is a real constant, Eq. (32) yields a solution $V(u,t) = v_0$ provided that $V_c(t)$ is defined by (39); see Appendix A. Obviously, the functions $f(t)$, $z_c(t)$, and, consequently, $V_c(t)$ and $F(t) = V_c(t)/f(t)$ are real valued.

In order to reduce the number of parameters, we rewrite the equation of motion for the fluid contour (32) in terms of the function $\xi_u(u,t)$,

$$\frac{\partial \xi_u}{\partial t} = \frac{\partial}{\partial u}\left[\xi_u(\hat{H} - i)\frac{\hat{H}\Psi_u}{|\xi_u|^2} - 2F(t)\xi_u \sin u\right]. \tag{40}$$

Separating the real part of Eq. (40), we derive the equation sought for

$$\frac{\partial \varsigma_u}{\partial t}=\frac{\partial}{\partial u}\left[\varsigma_u\left(\hat{H}\frac{\hat{H}\Psi_u}{\varsigma_u^2+(\hat{H}\varsigma_u)^2}-2F(t)\sin u\right)+\frac{(\hat{H}\varsigma_u)(\hat{H}\Psi_u)}{\varsigma_u^2+(\hat{H}\varsigma_u)^2}\right]. \tag{41}$$

The imaginary part of ξ, $\lambda(u,t)$, is found from (6).

C. Equation for the velocity potential

The partial time derivative of the contour function (15) $\Psi(u,t)$ is expressed via the time derivative of the complex velocity potential $X(z,t)$ on the boundary contour $\xi(u,t)$,

$$\frac{\partial}{\partial t}\Psi(u,t)=\frac{\partial}{\partial t}\mathrm{Re}\left[X(\xi(u,t),t\right]=\left.\frac{\partial \Phi}{\partial t}\right|_{z=\xi}+\mathrm{Re}\left[\left.\frac{\partial X}{\partial z}\right|_{z=\xi}\frac{\partial \xi}{\partial t}\right]. \tag{42}$$

In the interior of the domain $\Re(t)$ the dynamics of the incompressible inviscid fluid is described by the Bernoulli integral

$$\frac{\partial}{\partial t}\Phi(z,t)+\frac{1}{2}|v(z,t)|^2+\frac{1}{\rho}P(z,t)=a(t), \tag{43}$$

where $P(z,t)$ is the pressure of the fluid, ρ is the constant fluid density, and $a(t)$ is some function of time. We can express the time derivative of the velocity potential on the boundary contour from (43),

$$\left.\frac{\partial \Phi}{\partial t}\right|_{z=\xi}=a(t)-\frac{1}{2}(v_{||}^2+v_{\perp}^2)-\frac{p}{\rho}, \tag{44}$$

where $p(u,t)=P(\xi(u,t),t)$ is the fluid pressure on the boundary contour $\xi(u,t)$. On the other hand, the second term on the right-hand side of (42) is a scalar product of two complex vectors, $v(\xi(u,t),t)$ and $V(u,t)$,

$$\mathrm{Re}\left[\left.\frac{\partial X}{\partial z}\right|_{z=\xi}\frac{\partial \xi}{\partial t}\right]=v_{||}V_{||}+v_{\perp}V_{\perp}. \tag{45}$$

Substituting Eqs. (44) and (45) into (42), we obtain an evolution equation for the contour function $\Psi(u,t)$,

$$\frac{\partial \Psi}{\partial t}=a(t)+\Psi_u\left(\hat{H}\frac{\hat{H}\Psi_u}{\varsigma_u^2+(\hat{H}\varsigma_u)^2}-2F(t)\sin u\right)+\frac{1}{2}\frac{(\hat{H}\Psi_u)^2-\Psi_u^2}{\varsigma_u^2+(\hat{H}\varsigma_u)^2}-\frac{p}{\rho}. \tag{46}$$

The yet unknown function of time, $a(t)$, vanishes from the equation for the evolution of the derivative, $\Psi_u(u,t)$,

$$\frac{\partial \Psi_u}{\partial t}=\frac{\partial}{\partial u}\left[\Psi_u\left(\hat{H}\frac{\hat{H}\Psi_u}{\varsigma_u^2+(\hat{H}\varsigma_u)^2}-2F(t)\sin u\right)+\frac{1}{2}\frac{(\hat{H}\Psi_u)^2-\Psi_u^2}{\varsigma_u^2+(\hat{H}\varsigma_u)^2}-\frac{p}{\rho}\right]. \tag{47}$$

Equations (41) and (47) form a closed system of integro-differential equations, which describe the evolution of the contour functions, $\varsigma_u(u,t)$ and $\Psi_u(u,t)$. Evolution of this system satisfies the following conservation law:

$$\frac{d}{dt}\oint_{z=\xi}\Phi dz+\oint_{z=\xi}\frac{P}{\rho}dz=0, \tag{48}$$

which ensures conservation of the total momentum of the system, see Appendix B.

The perfectly conducting fluid approximation means that the magnetic field does not penetrate into the plasma column, and the electric current is concentrated in the infinitely thin skin layer adjacent to the boundary contour $\xi(u,t)$ with surface density $J(u,t)$. Each wire carries $1/N$ of the total current $I(t)$, which is expressed by the normalization condition

$$\int_0^{2\pi}J(u,t)|\xi_u(u,t)|du=\frac{I(t)}{N}. \tag{49}$$

In the exterior vicinity of the contour, only the longitudinal component of the magnetic field is induced by the electric current

$$\mathbf{B}(z,t)\big|_{z\to\xi(u,t)}=\mathbf{e}_{||}B_{||}(u,t),\quad z\notin\Re(r), \tag{50}$$

where

$$B_{||}(u,t)=\mu_0 J(u,t). \tag{51}$$

The sum of magnetic and hydrodynamic pressure should be continuous through the thin skin layer, hence the fluid pressure under the skin layer is determined by the local surface current density

$$p(u,t)=\frac{1}{2\mu_0}B_{||}^2(u,t)=\frac{\mu_0}{2}J^2(u,t). \tag{52}$$

The procedure for calculating the distribution of current density $J(u,t)$ for any given contour $\xi(u,t)$ is described in the next section.

We have shown that the 2D dynamics of the wire plasma in this model is described by two coupled 1D integro-differential evolution equations (41) and (47). It must be supplemented by the procedure of determining the distribution of current density on the surface of the plasma column self-consistently for its given position and the shape of its horizontal cross section.

Our approach has much in common with one developed in Ref. 19. Regularization of the singularity at $z_0=0$ is done differently here, which makes it possible for us to update the numerical solution for a longer time. The original formalism of Ref. 19 would not be applicable here for a wire displacement exceeding its initial diameter: the singularity would move through the boundary contour. The system of hydrodynamic equations derived in Ref. 19 contained three equations, with two of them being harmonically conjugated. For this system, we were unable to obtain a stable numerical solution even using a Lax–Friedrichs scheme with the highest possible numerical dissipation. Such a system does not seem to be similar to a hyperbolic system of conservation equations. On the other hand, our system of two equations (41) and (47) has two characteristic velocities (Alfvén veloc-

ity with positive and negative signs), and in this sense resembles a hyperbolic system. Its numerical integration is sufficiently simple.

Some mathematical methods developed for the study of interfacial hydrodynamic instabilities[21] were used in the derivations presented in the Appendixes.

III. MAGNETOSTATICS

A. Equation and boundary conditions for the magnetic vector potential

The results of Sec. II apply to an arbitrary 2D potential motion of a perfectly conducting, incompressible fluid. Here we use the Nth order rotational symmetry to find the distribution of current on the surface of each plasma column, and hence, the magnetic pressure that drives the implosion.

The magnetic field $\mathbf{B}$ is expressed via the vector potential $\mathbf{A}$,

$$\mathbf{B}=\boldsymbol{\nabla}\times\mathbf{A}, \quad \boldsymbol{\nabla}\cdot\mathbf{A}=0. \tag{53}$$

Neglecting the displacement currents, we arrive to the quasistatic (in our particular case, magnetostatic) approximation: from the Maxwell equation $\boldsymbol{\nabla}\times\mathbf{B}=\mu_0\mathbf{J}$, in vacuum, where there is no current density, and (53), we find that the magnetic vector potential satisfies the Laplace equation:

$$\boldsymbol{\nabla}^2\mathbf{A}=0. \tag{54}$$

If the current density $\mathbf{J}$ is directed along the wires, as is the case for a wire array without axial magnetic field, then the vector potential has only one nonzero component in the same direction, $A(z,t)$, where, as above, $z=x+iy$. The magnetic field $\mathbf{B}=B_x\mathbf{e}_x+B_y\mathbf{e}_y$, where

$$B_x=\frac{\partial A}{\partial y} \quad \text{and} \quad B_y=-\frac{\partial A}{\partial x}. \tag{55}$$

The current density is assumed below to be composed of a large number of discrete thin current filaments. Therefore, $A(z,t)$ is a real part of an analytic function with a large number of logarithmic singularities located at the positions of the current filaments.

The wire array is enclosed in a cylindrical, perfectly conducting return current can, whose radius is R_r. The vector potential of the return current can is assumed zero. The value of the vector potential at the surface of the plasma columns, $A(\xi,t)=\Lambda(t)$ has a clear physical meaning,

$$\phi=\int \mathbf{B}\cdot d\mathbf{S}=-l\int \frac{\partial A}{\partial r}dr=l\Lambda(t) \tag{56}$$

and

$$\frac{d}{dt}\phi=l\frac{d}{dt}\Lambda(t)=-\int [\nabla\times\mathbf{E}]\cdot d\mathbf{S}=U, \tag{57}$$

where ϕ is the magnetic flux, l is the length of the wire array, U is the voltage applied to it. The integration contour in Eqs. (56) and (57) consists of two parallel straight lines, one on the plasma column surface, another on the return current can surface. For a single conductor carrying a current I inside a return current can, the inductance per unit length is defined as

$$\frac{L}{l}=\frac{\phi}{Il}=\frac{\Lambda(t)}{I}. \tag{58}$$

Direct calculation of the energy integral gives

$$W=\frac{1}{2\mu_0}\int B^2\,dV=\frac{1}{2}\frac{(l\Lambda)^2}{L}, \tag{59}$$

which illustrates that the inductance is positive definite.[22] This is readily generalized for a system of parallel straight conductors inside the same return current can. Then instead of Eq. (58) we obtain

$$L_{jk}I_k=l\Lambda_j. \tag{60}$$

(Here and below, summation over repeated indices is implied.) The inductance matrix L_{jk} is symmetric and positive definite.[22] Such a matrix can always be inverted, and efficient numerical methods for its inversion are available.

B. Vector potential of current filaments in a cylindrical can

Introduce an elementary current $\delta I_n(u,t)$ flowing in the interval $[u-\delta u/2,u+\delta u/2]$ of the contour $\xi_n(u,t)$. Due to the rotational symmetry, $\delta I_n(u,t)=\delta I(u,t)$ (recall that the subscript referring to the first contour is omitted). The current filament δI_n generates the magnetic vector potential satisfying the boundary condition $\delta A_n(z,t)=0$ at the return current can, $|z|=R_r$,

$$\delta A_n=\mathrm{Re}(\delta Y_n)=\frac{\mu_0}{2\pi}\delta I_n\,\mathrm{Re}\left[\ln\frac{R_r^2-\overline{\xi}_n z}{R_r(z-\xi_n)}\right]$$
$$=\frac{\mu_0}{2\pi}\delta I\ln\frac{|R_r^2-\overline{\xi}_n z|}{R_r|z-\xi_n|}. \tag{61}$$

Here, the magnetic vector potential generated by a single elementary filament is presented as a real part of a function δY_n which is analytic in the exterior of the conducting contour $\xi_n(u,t)$. This feature of Eq. (61) helps in summation of the corresponding contributions from all the other wires in the array. Taking into account that

$$\prod_{n=1}^{N}\left[z-\xi\exp\left(2\pi i\frac{n-1}{N}\right)\right]=z^N-\xi^N, \tag{62}$$

we obtain

$$\delta A(z,t)=\sum_{n=1}^{N}\delta A_n=\frac{\mu_0}{2\pi}\delta I\ln\frac{|R_r^{2N}-(\overline{\xi}z)^N|}{R_r^N|z^N-\xi^N|}. \tag{63}$$

For large number of wires, the inequality $(|\xi|/R_r)^N\ll 1$ is satisfied, so that Eq. (63) reduces to

$$\delta A(z,t)=\frac{\mu_0}{2\pi}\delta I\ln\frac{R_r^N}{|z^N-\xi^N|}. \tag{64}$$

This approximation can be used if the plasma column is not too close to the return current can.

The vector potential δA given by (63) is the real part of an analytic function δY. Equation (63) could be used to de-

termine the distribution of return current density on the can surface, $J_r(\varphi,t)$, where φ is the coordinate on this surface: $z=R_r e^{i\varphi}$,

$$\delta J_r=\frac{1}{\mu_0}\frac{\partial}{\partial r}\delta A=\frac{1}{\mu_0 R_r}\frac{\partial}{\partial\varphi}\mathrm{Im}(\delta Y)$$
$$=-\frac{N\delta I}{2\pi R_r}\frac{R_r^{2N}-|\xi|^{2N}}{|R_r^N-\xi^N\exp(-iN\varphi)|^2}. \quad (65)$$

The average density of the return current $\langle\delta J_r\rangle=-N\delta I/(2\pi R_r)$ corresponds to the total return current $-N\delta I$, which fully balances the elementary currents of all wires, as it should. The return current density varies between the minimum and maximum values equal to $\langle\delta J_r\rangle(R_r^N-|\xi|^N)/(R_r^N+|\xi|^N)$ and $\langle\delta J_r\rangle(R_r^N+|\xi|^N)/(R_r^N-|\xi|^N)$, respectively, where $r=|\xi|$ correspond to the center-of-mass position of the wires. The maximums are located exactly opposite the wires, the minimums are located between them. Variation of the return current density is negligible provided that $(|\xi|/R_r)^N\ll 1$, i.e., when the approximation (64) applies.

The total contribution to the vector potential from all the contour currents could be found from integrating (63) over the coordinate u,

$$A(z,t)=\frac{\mu_0}{2\pi}\int_0^{2\pi}J|\xi_u|\ln\frac{|R_r^{2N}-(\bar{\xi}z)^N|}{R_r^N|z^N-\xi^N|}du. \quad (66)$$

Substitution of (66) into the boundary condition for the magnetic vector potential on the plasma column $A(\xi,t)=\Lambda(t)$ yields the integral equation

$$\Lambda(t)=\frac{\mu_0}{2\pi}\int_0^{2\pi}J|\xi_u|\ln\frac{|R_r^{2N}-[\bar{\xi}(u,t)\xi(w,t)]^N|}{R_r^N|\xi(w,t)^N-\xi(u,t)^N|}du \quad (67)$$

which holds for any w between 0 and 2π. Solving (67) for the current density $J(u,t)$ and applying the normalization condition (49), we find both the distribution of the current density and the inductance from Eq. (58). The return current density $J_r(\varphi,t)$ is expressed as

$$J_r(\varphi,t)=-\frac{N}{2\pi R_r}\int_0^{2\pi}\frac{J|\xi_u|(R_r^{2N}-|\xi|^{2N})}{|R_r^N-\xi^N\exp(-iN\varphi)|^2}du. \quad (68)$$

C. Thin-wire approximation for single and nested arrays

Before describing a general method that we use for solving the integral equation (67), consider an important approximation which assumes the current to be uniformly distributed over the surface of a thin cylindrical conductor whose radius is R_w, i.e.,

$$\xi=R_c+R_w\exp(iu) \quad (69)$$

and $J|\xi_u|=I/2\pi N$. Here, R_c is the distance from the wire axis to the axis of symmetry of the array. The thin-wire approximation is valid if $R_w\ll R_c/N$, R_r-R_c. Then, of course, $R_w\ll R_c$, hence the numerator of argument of logarithmic function in Eq. (67) is approximated by $R_r^{2N}-R_c^{2N}$, whereas the denominator becomes $NR_c^{N-1}R_wR_r^N$. Thus we obtain the well-known Russell's formula[23] for the inductance of a single wire array

$$L=\frac{\mu_0 l}{2\pi}\left[\ln\frac{R_r}{R_c}+\frac{1}{N}\ln\frac{R_c}{NR_w}+\frac{1}{N}\ln\left\{1-\left(\frac{R_c}{R_r}\right)^{2N}\right\}\right]. \quad (70)$$

(It should be noted that a version of this formula presented in Ref. 24 contains a typographical error reproduced later by some other authors: instead of the radius of the wire, the second term in square brackets contains the wire diameter.) The correction of order of $(R_c/R_r)^{2N}$ was taken into account in Ref. 18. In most cases, it is very small.

Now consider a nested wire array, a load configuration initially suggested in Ref. 8 and then used in Refs. 1 and 16 and many other experiments. Here we consider two concentric rows each containing N wires located at the radii R_{c1} and R_{c2}, where subscripts 1 and 2 refer to the outer and inner arrays, respectively. Denote the complex coordinates of the first wires in each array by ξ_1 and ξ_2, respectively,

$$\xi_j=R_{cj}+R_{wj}\exp(iu),\quad j=1,2. \quad (71)$$

Vector potential of the global magnetic field in the case of nested wire array configuration is a sum of contributions from the two arrays

$$A(z,t)=A_1(z,t)+A_2(z,t), \quad (72)$$

where

$$A_j(z,t)=\frac{\mu_0}{2\pi}\int_0^{2\pi}J_j|\xi_{ju}|\ln\frac{|R_r^{2N}-(\bar{\xi}_j z)^N|}{R_r^N|z^N-\xi_j^N|}du. \quad (73)$$

Since both arrays are connected to the same electrodes, the magnetic vector potential has the same value for all the wires,

$$A(\xi_j,t)=\Lambda_j(t)=\Lambda(t),\quad j=1,2. \quad (74)$$

This condition allows one to find the distribution of current I between the inner and the outer components of the nested array, $I_1+I_2=I$. Applying the thin-wire approximation to both arrays (i.e., assuming $R_{wj}\ll R_{ck}$, $j,k=1,2$, and $J_j|\xi_{ju}|=I_j/2\pi N$), one can present the system of Eq. (60) in a matrix form

$$\hat{e}_j\phi=\hat{e}_j\int U\,dt=\hat{e}_j l\Lambda=\frac{\mu_0 l}{2\pi}\hat{L}_{jk}I_k,\quad j,k=1,2, \quad (75)$$

where $\hat{e}_j=\binom{1}{1}$ is the unit column and $\hat{L}_{jk}$ are the elements of the dimensionless inductance matrix

$$\hat{L}_{jj}=\ln\frac{R_r}{R_{cj}}+\frac{1}{N}\ln\left[\frac{R_{cj}}{NR_{wj}}\left(1-\frac{R_{cj}^{2N}}{R_r^{2N}}\right)\right],$$
$$\hat{L}_{jk}=\frac{1}{N}\ln\frac{R_r^{2N}-R_{cj}^N R_{ck}^N}{R_r^N|R_{cj}^N-R_{ck}^N|},\quad j\neq k. \quad (76)$$

Here, the diagonal elements of the matrix are self-inductances of the component arrays, and the off-diagonal term is the mutual inductance (in this case of a 2×2 matrix, the mutual inductance is $\hat{L}_{12}=\hat{L}_{21}$). The inductance matrix is

symmetric and positive definite,[22] thus the inverted matrix $\hat{L}_{jk}^{-1}$ always exists. Presenting the normalization condition in a vector form

$$I=I_j\hat{e}_j=I_1+I_2, \tag{77}$$

we obtain a general solution of Eqs. (75) and (77),

$$I_k=\frac{2\pi\phi}{\mu_0 l}\hat{L}_{jk}^{-1}\hat{e}_j. \tag{78}$$

The total inductance is

$$L=\frac{\phi}{I}=\frac{\mu_0 l}{2\pi}\frac{1}{\hat{e}_k\hat{L}_{jk}^{-1}\hat{e}_j} \tag{79}$$

and combining this with (78), we find

$$I_k=I\frac{\hat{L}_{jk}^{-1}\hat{e}_j}{\hat{e}_k\hat{L}_{jk}^{-1}\hat{e}_j}. \tag{80}$$

All the derivations for the nested arrays were performed in a general vector form, and therefore are valid for any amount of wires in arrays consistent with the *N*th order rotational symmetry (for instance, *N* wires in the inner and *2N* wire in the outer array).

For an important particular case when $(R_{c1}/R_r)^N, (R_{c2}/R_r)^N \ll 1$ we can further simplify (76) to give

$$\hat{L}_{11}=\ln\frac{R_r}{R_{c1}}+\frac{1}{N_1}\ln\frac{R_{c1}}{N_1R_{w1}},\quad \hat{L}_{22}=\ln\frac{R_r}{R_{c2}}+\frac{1}{N_2}\ln\frac{R_{c2}}{N_2R_{w2}},$$
$$\hat{L}_{12}=\hat{L}_{21}=\ln\frac{R_r}{R_{c1}}. \tag{81}$$

In the thin-wire approximation, Eq. (81) is valid under above assumptions for arbitrary numbers of wires N_1 and N_2 in the component arrays. The self-inductance for each of them is given by the Russell's formula. The mutual inductance in this approximation simply equals a self-inductance of a conducting shell whose radius equals the radius of the outer array. Physically, this is quite clear: the outer array generates the same magnetic flux in the contour formed by the inner array and the return current can as a conducting shell of the same radius R_{c1} would.

For a two-component nested wire array, the solutions (79) and (80) could be presented in a scalar form

$$L=\frac{\mu_0 l}{2\pi}\frac{\hat{L}_{11}\hat{L}_{22}-\hat{L}_{12}^2}{\hat{L}_{11}+\hat{L}_{22}-2\hat{L}_{12}},$$
$$I_1=I\frac{\hat{L}_{22}-\hat{L}_{12}}{\hat{L}_{11}+\hat{L}_{22}-2\hat{L}_{12}},\quad I_2=I\frac{\hat{L}_{11}-\hat{L}_{12}}{\hat{L}_{11}+\hat{L}_{22}-2\hat{L}_{12}}. \tag{82}$$

Using the approximation (81) for the self- and mutual inductance, one determines the fraction of the total current flowing in the inner array to be

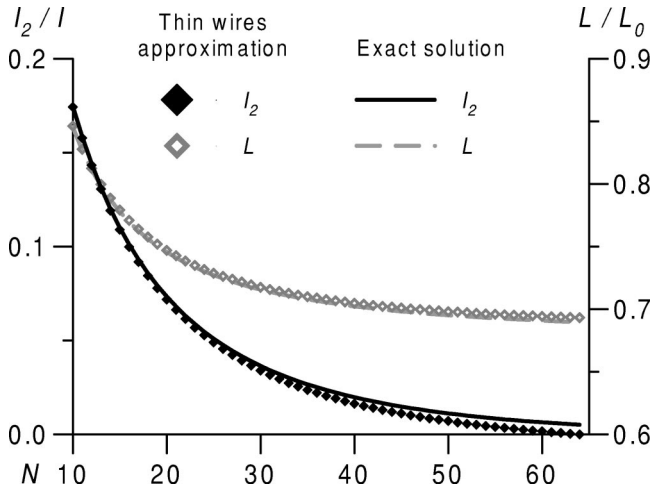

FIG. 2. Fraction of current in the inner array I_2/I and normalized inductance of the nested array L/L_0 ($L_0=\mu_0 l/2\pi$) vs number of wires in both arrays, *N*, for $R_r/R_{c1}=2$, $R_{c1}/R_{c2}=2$, $R_{c1}/R_{w1}=R_{c2}/R_{w2}=64$. Lines represent exact values found numerically, symbols—the thin-wire approximation.

$$\frac{I_2}{I}=\frac{\frac{1}{N_1}\ln\frac{R_{c1}}{N_1R_{w1}}}{\ln\frac{R_{c1}}{R_{c2}}+\frac{1}{N_1}\ln\frac{R_{c1}}{N_1R_{w1}}+\frac{1}{N_2}\ln\frac{R_{c2}}{N_2R_{w2}}}. \tag{83}$$

According to (81), the numerator of the right-hand side of (83) is the excess of the self-inductance of the outer array over the self-inductance of a perfectly conducting shell of the same radius R_{c1}. A perfectly conducting shell would provide a perfect screening, $I_2=0$. Equation (83) also implies that a perfect screening—no current in the inner array—is achieved when the argument of the logarithm is unity, i.e., the gap-to-diameter ratio is

$$\frac{r_g}{D_{w1}}=\pi, \tag{84}$$

where $r_g=2\pi R_1/N_1$ is the gap between the centers of the neighboring wires, $D_{w1}=2R_{w1}$ is the outer wire diameter. In fact, the current in the inner array does not vanish when (84) is satisfied, see below. Rather, Eq. (84) indicates the gap-to-diameter ratio below which the thin-wire approximation is no longer valid. For typical experimental conditions of, say, Ref. 1 ($N_1=240$, $N_2=120$, $R_{c1}=2$ cm, $R_{c2}=1$ cm, R_{w1} and R_{w2} varied between 20 and 50 μm), the current fraction in the inner array varies between 0.8% and 0.3%. Our explicit expressions for self- and mutual inductance of single and nested wire arrays can help in obtaining a simple zero-dimensional (0D) description of their implosion dynamics, see Appendix C.

Figure 2 compares the current fraction in the inner array and the total induction found using the thin-wire approximation and with the aid of Eq. (74) solved exactly, as described in the next section. Here $R_r/R_{c1}=2$, $R_{c1}/R_{c2}=2$, $R_{c1}/R_{w1}=R_{c2}/R_{w2}=64$, and the number of wires in both arrays, $N_1=N_2=N$ is varied. The condition (84) corresponds to $N=64$. We see that (83) is a good approximation for I_2/I up to $N\sim 50$. For larger number of wires, this approximation

breaks down for the obvious reason: distribution of the current density on the surface of a conducting plasma column cannot be assumed uniform when the distance between the neighboring columns is comparable to the column diameter. Note that the expression for the total inductance L remains a good approximation even when the thin-wire approximation becomes formally invalid.

D. Arbitrary shape of the boundary contour: Distribution of current in discrete filaments

The technique described in Sec. III C allows us to develop a general method of calculating the current density distribution on the surface of a conductor with arbitrary shape of its cross section. For this, we approximate the conducting surface with a large number of thin current filaments and treat these filaments as separate wires connected in parallel to the same electrodes. Therefore, all these filaments are at the same vector potential. Assuming the radii of these filaments much less than the cross-sectional dimension of the plasma column, R_w, one can use the symmetrical, positive–definite inductance matrix derived above in the thin-wire approximation to determine the distribution of the current between the filaments.

Here we describe this calculation for a single wire array (it is readily generalized for a nested wire array). The interval $[0,2\pi]$ for the variable u is split into a large number $K \gg 1$ of subintervals $[u_k-(1/2)\Delta u, u_k+(1/2)\Delta u]$, where $\Delta u = 2\pi/K$. It is assumed that the complex coordinate of the middle point of the kth subinterval $\xi_k(t)=\xi(u_k,t)$ defines the position of the kth filament, which carries a current $I_k = J(u_k,t)|\xi_{ku}|\Delta u$, and its effective radius is $q_k = (1/2)|\xi_{ku}|\Delta u \ll R_w$. Thus the solution (75) obtained in the thin-wire approximation, remains valid,

$$\hat{e}_j \phi = \hat{e}_j l\Lambda = \frac{\mu_0 l}{2\pi}\hat{L}_{jk} I_k, \quad j,k=1,\ldots,K, \tag{85}$$

where $\hat{e}_j$ is now a unit column containing K rows. The inductance matrix is similar to (76), but its elements now refer to the current filaments on the surface of a single plasma column rather than to the inner and outer components of a nested wire array,

$$\begin{aligned} \hat{L}_{jj} &= N \ln\frac{R_r}{|\xi_j|} + \ln\left[\frac{|\xi_j|}{Nq_j}\left(1-\frac{|\xi_j|^{2N}}{R_r^{2N}}\right)\right], \\ \hat{L}_{jk} &= \ln\frac{|R_r^{2N}-(\bar{\xi}_k\xi_j)^N|}{R_r^N|\xi_j^N-\xi_k^N|}, \quad j\neq k. \end{aligned} \tag{86}$$

The normalization condition (77) becomes

$$NI_k\hat{e}_k = I. \tag{87}$$

The total inductance of the N-wire array is given by an equation similar to (79),

$$L = \frac{\mu_0 l}{2\pi N}\frac{1}{\hat{e}_k\hat{L}_{jk}^{-1}\hat{e}_j} \tag{88}$$

and the current in each filament is given by a formula similar to (80),

$$I_k = \frac{I}{N}\frac{\hat{L}_{jk}^{-1}\hat{e}_j}{\hat{e}_k\hat{L}_{jk}^{-1}\hat{e}_j}. \tag{89}$$

Using the formulas (86)–(88) and (89), the distribution of the current density on the surface of a conductor with arbitrary shape of its cross section can be calculated numerically. In the plasma dynamics problem described in Sec. II, the cross section is represented by a given contour $\xi(u,t)$ on a complex plane. We can thus find the fluid pressure in Eq. (52) $p=p_k=p(u_k,t)$ for the given complex coordinate $\xi_k(t)=\xi(u_k,t)$ of a boundary contour,

$$p(u_k,t) = \frac{\mu_0}{2}J^2(u_k,t) = \frac{\mu_0}{2}\frac{I_k^2}{(\Delta u)^2}\frac{1}{|\xi_u(u_k,t)|^2}. \tag{90}$$

This closes the MHD model presented in this paper.

IV. DYNAMICS OF A SINGLE WIRE ARRAY IMPLOSION

We apply dicretization to both arguments u and t of the contour functions $\xi_u(u,t)$ and $\Psi_u(u,t)$. Numerical integration of Eqs. (41) and (47) is performed using a space-centered explicit predictor–corrector Lax–Wendroff scheme of second order. The integral operator $\hat{H}$ is calculated using the algorithm of fast Fourier transform (see Appendix D for details).

The wire array is characterized by its effective radius $R_c(t)$ [associated with the position of the point $z_c(t)$ introduced by Eq. (38)], the average radius $R_w(t)$ of the conducting contour $\xi(u,t)$ representing the cross section of a plasma column, the number N of wires in the array, and the radius R_r of the return current can. The initial shape of the domain $\Re(t=0)$ is a circle with the radius $R_w(0)$, whose center is on the real axis at $x=R_c(0)$. Our model equations could be coupled to an arbitrary circuit equation, but here we assume the current driver to be sufficiently stiff, so that the current wave form is independent from the implosion dynamics and could be presented as

$$I(t) = I_{\max}\sin^2\left(\frac{\pi t}{2t_{\max}}\right). \tag{91}$$

This approximation is good for the experiments on the MAGPIE facility in the Imperial College;[14–16] for MAGPIE, $I_{\max}$ varies between 1 and 1.4 MA, and $t_{\max}$ is about 240 ns. We choose the initial parameters close to (but not exactly the same as) those of the MAGPIE experiments. The initial radius of the wire array is taken to be $R_c(0)=8$ mm, the radius of the plasma corona after the explosion of a 15 μm Al wire $R_w(0)=125$ μm, $t_{\max}$ is taken between 250 and 300 ns, the number of wires in the array is varied from 8 to 64. The radius of the cylindrical return current can, $R_r=10$ mm, is intentionally taken much less than that of the return current structure of MAGPIE (4 to 8 posts at about 75 mm from the axis). The corresponding ratio that we have chosen, $R_r/R_c(0)=1.25$, is more typical for "Z" and other multi-MA generators, which are softer than MAGPIE and thereby require low-inductance loads. Proximity of the return

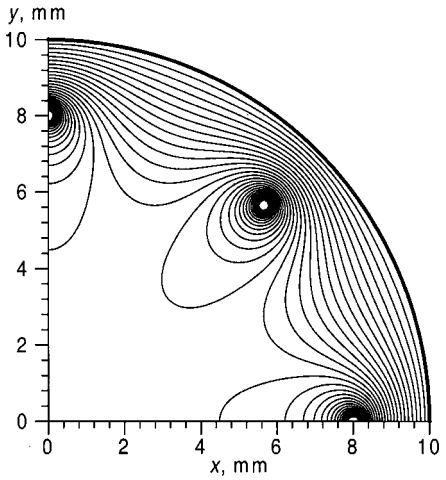

FIG. 3. Magnetic force lines for a 8-wire array with $R_w(0)=125$ μm, $R_c(0)=8$ mm, $R_r=10$ mm, at early time $t\to+0$, before the motion and deformation of the array started. Bold lines show the conducting contours ξ_1,ξ_2,ξ_3 and the return current can.

current structure to the imploded wire array can make the nonuniformity of the return current an issue, which we are going to address below.

The main parameter determining the configuration of magnetic field in the wire array is the gap-to-diameter ratio $\pi R_c(0)/NR_w(0)$, cf. Eq. (84). If $N=8$ this parameter is large enough, about 25. In this case, as shown in Fig. 3, a substantial part of the magnetic flux penetrates the interwire gaps towards the axis of the array. Figure 4 shows that the current density tends to be concentrated on the outer part of the plasma column surfaces (peaking at $u=0$), although its distribution is close to uniform: $J(\pi)/J(0)\approx 80\%$.

In the other limit $N=64$ (Fig. 5) the neighboring conducting contours are close, $\pi R_c(0)/NR_w(0)=\pi$, and the

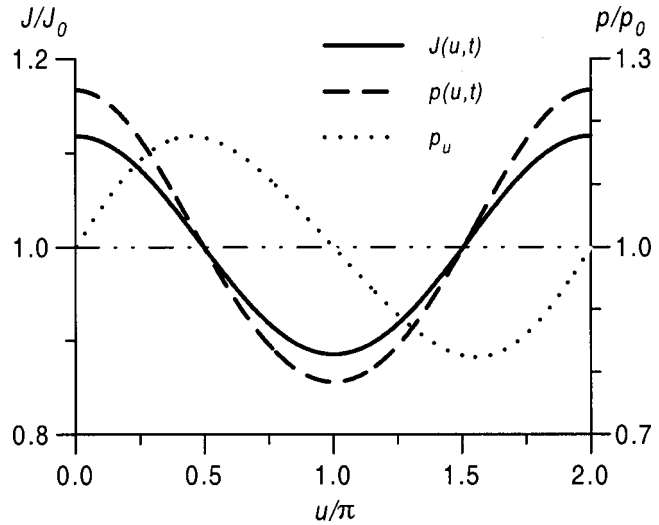

FIG. 4. Relative variation of the current density $J(u,t)$ and fluid pressure $p(u,t)$ normalized to $J_0=I(t)/2\pi NR_w$ and $p_0=\mu_0 J_0^2/2$, respectively, vs the contour parameter u, for the conditions of Fig. 3. The derivative $p_u=\partial p/\partial u$ is also shown in arbitrary units with its zero level marked by the dashed–dotted line. The positions defined as $u=0$ and $u=\pi$ correspond to points of the contour, which are farthest from and closest to the axis, respectively (cf. Fig. 1).

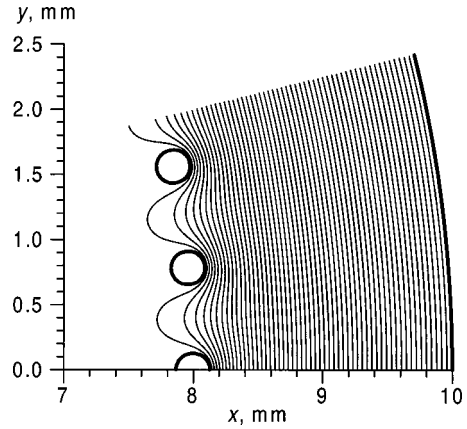

FIG. 5. Same as in Fig. 3 for a 64-wire array with $R_w(0)=125$ μm, $R_c(0)=8$ mm, $R_r=10$ mm.

magnetic field is effectively screened from penetration through the gaps between the plasma columns. In this case most of the current flows through the outer area of the conducting surface (Fig. 6): $J(\pi)/J(0)=12\%$, and, consequently, $p(\pi)/p(0)=1.4\%$.

Figure 7 shows that the distribution of the current density $J_r(\varphi)$ on the return current can surface is not uniform due to proximity of the plasma columns to the can wall. The function $J_r(\varphi)$ has N maximums at $\varphi=2\pi(n-1)/N$, $n=1,...,N$, just opposite to the plasma columns. If the return current radius is increased to 20 mm, then the distribution of the return current becomes almost uniform, whereas the distribution of current density on the plasma surface would remain virtually unchanged.

The periodic pressure function $p(u,t)$ shown in Figs. 4 and 6 is expanded into the Fourier series

$$p(u,t)=p_0(t)+p_1(t)\cos u+p_2(t)\cos 2u+\cdots. \qquad (92)$$

The first term in the expansion (92), $p_0(t)$ describes a uniform pressure distribution. This corresponds to the contribution to the pressure provided by the ''private'' magnetic filed

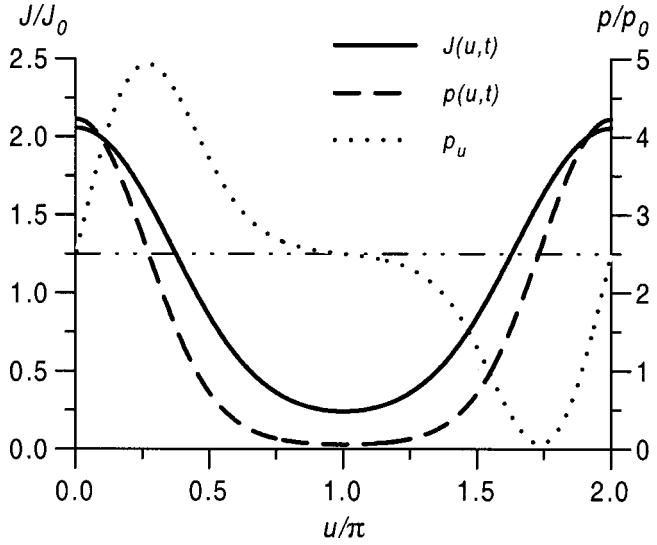

FIG. 6. Same as in Fig. 4, for the conditions of Fig. 5.

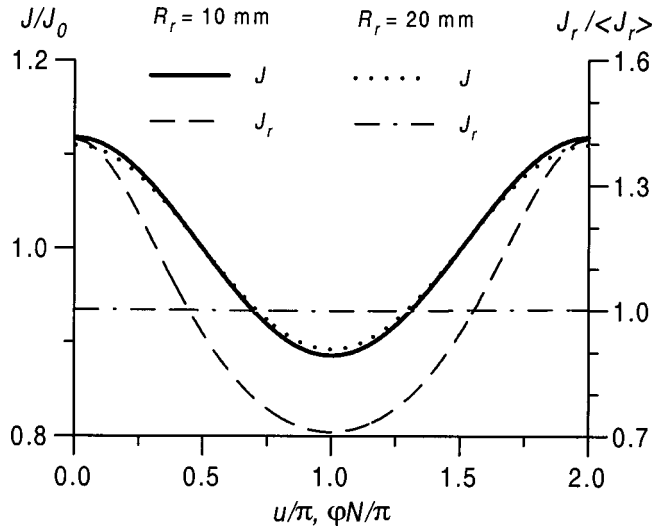

FIG. 7. Relative variation of the current density $J(u,t)$, normalized as in Fig. 4, and of the return current density $J_r(\varphi,t)$ [normalized with respect to $\langle J_r\rangle = I(t)/2\pi R_r$], for the conditions of Fig. 3, and the same for the radius of return current can $R_r = 20$ mm.

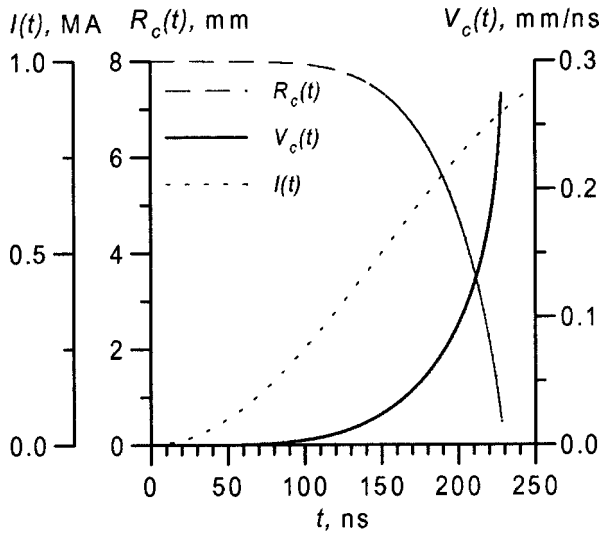

FIG. 8. Implosion dynamics of a wire array whose initial configuration is shown in Fig. 3: the average radius of the array $R_c(t)$, the implosion velocity $V_c(t) = |\dot{R}_c(t)|$ and the current wave form $I(t)$.

of the individual wire, which would result in its pinching if it were compressible. Obviously, this component does not change the shape of the boundary contour and causes no acceleration of the plasma column.

The second term, $p_1(t)\cos u$, is due to the force that is responsible for the implosion of the wire array. This force is caused by the interaction of the surface current with the global magnetic field and accelerates each wire towards the axis of the array [at all time, $p_1(t) > 0$] without affecting its cross-sectional shape.

The third component, $p_2(t)\cos 2u$, approximates the interaction between the surface current in the neighboring plasma columns by a local tidal force. This force deforms the boundary contour $\xi(u,t)$, squeezing it along the real x axis and expanding it along the imaginary y axis, without accelerating the plasma column as a whole. The tidal force causes the plasma columns to merge, to form a uniform shell during the implosion of the array.

Thus, dynamics of the plasma columns is defined by a competition between the implosion and tidal forces. The relative role of the tidal force could be estimated by the variable $p_{21}(t) = p_2(t)/p_1(t)$. This parameter is mostly affected by the gap-to-diameter ratio $\pi R_c(t)/NR_w(t)$ during the implosion.

We simulated the implosion of an 8-wire array, taking $I_{\max} = 1$ MA and $t_{\max} = 310$ ns in Eq. (91). At the initial moment $p_{21}(0) = 0.04$, and the implosion force dominates over the tidal force responsible for the annular shell formation. At the early stage of implosion, the plasma columns retain their initial circular shapes as they accelerate towards the axis. The function $R_r(t)$ shown in Fig. 8 reproduces the well-known 0D solution [cf. Appendix C, Eq. (C2)] for the implosion of a thin conducting shell driven by a current (91).

At the later stage of the implosion, as the gap-to-diameter ratio $\pi R_c(t)/NR_w(t)$ decreases, the tidal force gradually becomes dominant. Figure 9 shows that the deformation of the boundary contours becomes noticeable at $R_c \approx 1.2$ mm. At this point the gap-to-diameter ratio is about 2, and the magnetic field configuration is similar to one shown in Fig. 5. However, the wire plasmas by this moment already have a high inward radial velocity, and the shell formation is only completed when $R_c \approx 0.5$ mm.

In the case of a 64-wire array, the tidal force plays an important role from the very beginning: $p_{21}(0) = 0.36$. Figure 10 demonstrates that the column cross sections are already substantially deformed at the moment $t = t_{\max}/4$, when the columns have barely moved from their initial positions toward the axis of the array. The distributions of current den-

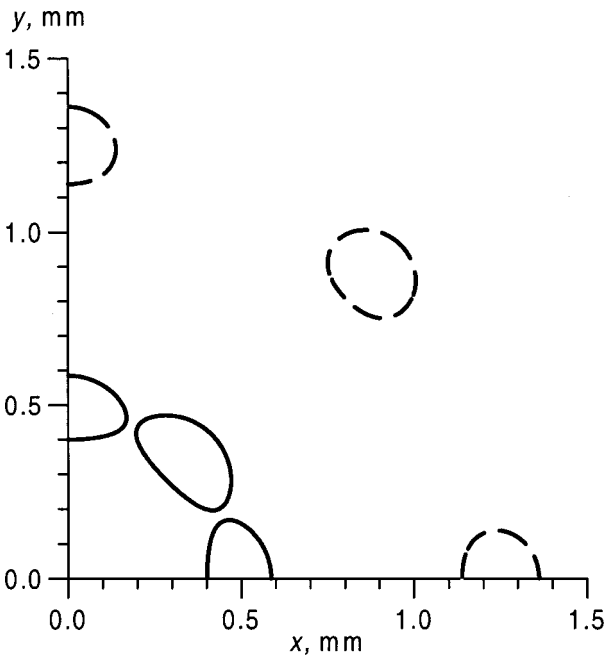

FIG. 9. Cross sections of the plasma columns ξ_1, ξ_2, and ξ_3 at the instants when $R_c(t) = 1.2$ mm (dashed lines) and 0.5 mm (solid lines) for the implosion whose time history is shown on Fig. 8.

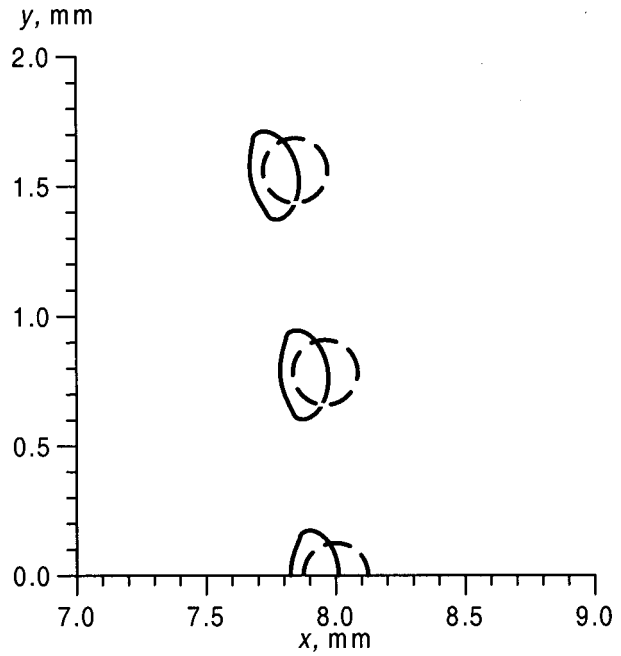

FIG. 10. Early-time implosion dynamics of a wire array whose initial configuration is shown in Fig. 5. Solid lines show the cross sections of the plasma columns ξ_1, ξ_2, and ξ_3 at $t=t_{\max}/4$; dashed lines refer to their initial shapes and positions at $t=0$.

sity and pressure at this moment shown in Fig. 11 are very close to the step functions characteristic of an annular shell implosion.

Our analysis demonstrated a competition between the imploding force, making the array implode as a set of individual wires, and the tidal force making the wires merge into an annular shell. Formation of precursor plasma streams flowing to the axis ahead of the main plasma mass is not described by the present model. The reason for this is seen from Eq. (50): only the normal component of the **J×B** force acts on the boundary surface of the plasma column, pushing

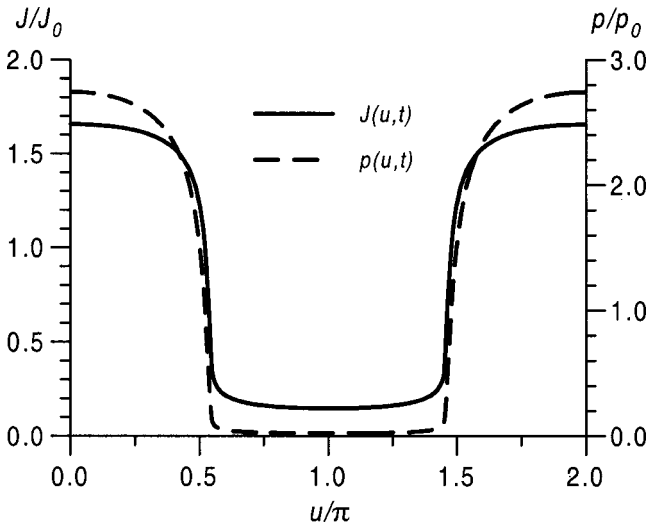

FIG. 11. Relative variation of the current density $J(u,t)$ and fluid pressure $p(u,t)$ normalized as in Fig. 4, for the contours shown by the solid lines in Fig. 10.

the plasma inward. It is well known, however, that the exploded wire plasma is highly nonhomogeneous. As predicted in Ref. 25 and confirmed in later studies (see Ref. 10 and references therein), electrical explosion of a solid wire produces a plasma column, which contains high-density core and low-density corona regions, with the skin depth comparable to the thickness of the corona. Assuming the corona thickness at early time much less than the core diameter, we can roughly estimate the longitudinal component of the **J×B** acting on some parts of the coronal plasma by

$$e_{||}\cdot[\mathbf{J}\times\mathbf{B}]\propto J(u,t)\frac{\partial}{\partial u}B_{||}(u,t)\propto\frac{\partial}{\partial u}p(u,t)\equiv p_u. \qquad (93)$$

Qualitative profiles of the derivative p_u are shown in Figs. 4 and 6. This function is zero at $u=0$ and $u=\pi$ and has two maximums near $u=\pi/2$ and $u=3\pi/2$. At both maximums of p_u the longitudinal component of the **J×B** force is directed to the axis of the wire array. Since the density of coronal plasma is much lower than the core density, and it is free to move away from the core, such a force configuration would produce precursor jets streaming to the pinch axis.[10,16] However, neither the process of generation nor the dynamics of these jets could be treated in the incompressible fluid approximation.

V. CONCLUSION

The implosion dynamics of wire arrays on the (r,θ) plane has been studied with the aid of a perfectly conducting, incompressible fluid model. The implosion dynamics is driven by the competition between the implosion pressure, which makes the array converge to the axis as a set of individual plasma columns, and the tidal pressure that makes the wires merge, forming an annular conducting shell. The relative roles of the implosion and tidal pressure are determined by the gap-to-diameter ratio $\pi R_c(t)/NR_w(t)$. If this ratio is large at early time (this is when the thin-wire approximation works, and the Russell's formula is valid), then the array implodes as a set of individual plasma columns. In the opposite limit, when this ratio is about π or less at early time, the thin-wire approximation is not applicable—the distribution of current over the plasma surface is very nonuniform, peaked at the outer side. Then the tidal forces prevail in the early-time dynamics, and the plasma columns tend to form a shell-like configuration before they start converging to the axis of the array.

The approximation of perfectly conducting incompressible fluid does not describe the precursor plasma jets that stream to the axis ahead of the heavier wire cores. These are driven by the longitudinal component of the **J×B** force, which we were able to estimate. This force peaks at the sides of the plasma columns and is directed to the axis of the array. To describe the jet formation on the (r,θ) plane, one therefore needs adequate models of the plasma conductivity and its equation of state.

Our model, being admittedly simplified, has the advantages of physical transparence and numerical efficiency. It could be used to benchmark the MHD hydrocodes on the (r,θ) plane, where no exact solutions were available for this

purpose until now. This model could also be applied to some other problems of relevance for the inertial confinement fusion. For instance, it could be used for modeling the nonlinear stages of Rayleigh–Taylor and Richtmyer–Meshkov instabilities, where it might have some advantages over the existing analytical and semianalytical approaches (see Refs. 26 and references therein).

ACKNOWLEDGMENTS

The authors are grateful to S. V. Lebedev, J. P. Chittenden, P. V. Sasorov, R. E. Terry, and L. I. Rudakov for valuable comments and suggestions.

A.L.V. was supported by the Defense Threat Reduction Agency. A.A.E. was supported by the JSPS fellowship (Grant No. P99268).

APPENDIX A: A PARTICULAR SOLUTION OF THE EQUATION OF MOTION FOR THE CONTOUR; UNIFORM VELOCITY

Complex velocity potential $X(z,t)=zv_0$, where v_0 is a real constant, corresponds to a uniform distribution of the fluid velocity: $v(z,t)=v_0$. In this case the boundary value Ψ of the velocity potential $\Phi(z,t)=v_0\,\mathrm{Re}(z)$ is

$$\Psi(u,t)=v_0\,\mathrm{Re}[\xi(u,t)],\quad \Psi_u=v_0\,\mathrm{Re}[\xi_u]. \tag{A1}$$

Substituting the above distribution of Ψ_u into Eq. (32), we obtain

$$\begin{aligned}
&\frac{\hat{H}\Psi_u}{|\xi_u|^2}=-v_0\,\mathrm{Im}\left(\frac{1}{\xi_u}\right),\\
&\hat{H}\frac{\hat{H}\Psi_u}{|\xi_u|^2}=v_0\,\mathrm{Re}\left(\frac{1}{\xi_u}\right)+\frac{2v_0}{f(t)}\sin u,\\
&V(u,t)=\xi_t=v_0+\frac{2\xi_u}{f(t)}[v_0-V_c(t)]\sin u.
\end{aligned} \tag{A2}$$

If the function $V_c(t)$ satisfies (39),

$$\mathrm{s}_t(0,t)=\mathrm{s}_t(\pi,t)=v_0,\quad V_c(t)=v_0. \tag{A3}$$

Thus $V(u,t)=v_0$ for any shape of the boundary contour $\xi(u,t)$.

APPENDIX B: INTEGRAL OF MOTION

Let us calculate the following integral:

$$\begin{aligned}
\mathcal{P}&=\frac{d}{dt}\oint_{z=\xi}\Phi\,dz+\oint_{z=\xi}\frac{P}{\rho}dz\\
&=\frac{d}{dt}\int_0^{2\pi}\Psi\xi_u\,du+\int_0^{2\pi}\frac{p}{\rho}\xi_u\,du\\
&=\int_0^{2\pi}\left[\xi_u\left(\frac{\partial\Psi}{\partial t}+\frac{p}{\rho}\right)-\Psi_u\xi_t\right]du.
\end{aligned} \tag{B1}$$

Substituting Eqs. (32) and (46) into (B1), we obtain that

$$\mathcal{P}=\int_0^{2\pi}\left[a(t)-\frac{(\Psi_u-i\hat{H}\Psi_u)^2}{2|\xi_u|^2}\right]\xi_u\,du. \tag{B2}$$

Obviously,

$$a(t)\int_0^{2\pi}\xi_u\,du=a(t)\oint_{z=\xi}dz\equiv 0 \tag{B3}$$

and

$$\xi_u\frac{(\Psi_u-i\hat{H}\Psi_u)^2}{|\xi_u|^2}=\left[\frac{\partial\overline{X}(\overline{z})}{\partial\overline{z}}\right]^2_{\overline{z}=\overline{\xi}}=[v(\overline{z},t)]^2_{z=\overline{\xi}}. \tag{B4}$$

If we change the argument of the antianalytic function $v(z,t)$ to its complex conjugate, this function becomes an analytic function $v(\overline{z},t)$ which satisfies the Cauchy–Riemann conditions. Thus, according to the Cauchy theorem,

$$\mathcal{P}=-\frac{1}{2}\oint_{\overline{z}=\xi}v^2(\overline{z},t)d\overline{z}=0. \tag{B5}$$

Therefore Eq. (48) holds during the evolution of the system described by Eqs. (41) and (47).

APPENDIX C: DYNAMICS OF SINGLE AND NESTED WIRE ARRAYS IN A THIN-WIRE APPROXIMATION

Our expressions for self- and mutual inductance lead to a simple 0D description of the implosion dynamics in a thin-wire approximation. Equations of motion are derived from a Lagrangian, which for a single wire array has the form

$$\mathcal{L}=\mathsf{K}-\mathsf{U}=\frac{m}{2}\dot{R}_c^2+\frac{L(R_c)}{2}I^2. \tag{C1}$$

Here, m is the mass of the array, K is its kinetic energy, U is the potential or free energy given by the formula $\mathsf{U}=-LI^2/2$ from Ref. 22. Substituting the Russell formula (70) into the Lagrange equation $(d/dt)(\partial\mathcal{L}/\partial\dot{R}_c)=\partial\mathcal{L}/\partial R_c$, we obtain the well-known 0D equation of motion

$$m\ddot{R}_c=\frac{I^2}{2}\frac{\partial L}{\partial R_c}=-\frac{\mu_0 l(N-1)}{4\pi N R_c}I^2 \tag{C2}$$

(the current I is treated here as an independent variable). Equation (C2) says that each wire is pushed to the axis by the Ampère force due to the interaction of its current, I/N, with the azimuthal magnetic field produced by the remaining $N-1$ wires. Note that the radial acceleration of the wires is given by (C2) even if the wires are not distributed equidistantly on a circle whose radius is R_c.

For a nested wire array, the corresponding Lagrangian is

$$\begin{aligned}
\mathcal{L}&=\frac{m_1}{2}\dot{R}_{c1}^2+\frac{m_2}{2}\dot{R}_{c2}^2+\frac{L(R_{c1},R_{c2})}{2}I^2\\
&=\frac{m_1}{2}\dot{R}_{c1}^2+\frac{m_2}{2}\dot{R}_{c2}^2+\frac{\mu_0 l}{4\pi}[\hat{L}_{11}(R_{c1})I_1^2\\
&\quad+2\hat{L}_{12}(R_{c1},R_{c2})I_1I_2+\hat{L}_{22}(R_{c2})I_2^2],
\end{aligned} \tag{C3}$$

where m_1 and m_2 are the masses of the two components of the wire array, and its inductance is given by Eqs. (81) and (82). In the ''transparent inner'' mode of interaction,[8,9,16] the imploding outer array 1 can penetrate inside the inner array

2, and their respective roles will then be reversed. To take this into account, we generalize the expression (81) for the mutual inductance,

$$\hat{L}_{12}(R_{c1},R_{c2})=\hat{L}_{21}(R_{c1},R_{c2})=\ln\frac{R_r}{\max(R_{c1},R_{c2})}. \quad \text{(C4)}$$

The equations of motion derived from (C3) with the aid of (81), (82), (C4) are

$$\begin{aligned} m_1\ddot{R}_{c1}&=\frac{\mu_0 l}{4\pi}I^2\frac{\partial}{\partial R_{c1}}L \\ &=\frac{\mu_0 l}{4\pi}\left(I_1^2\frac{\partial\hat{L}_{11}}{\partial R_{c1}}+2I_1I_2\frac{\partial\hat{L}_{12}}{\partial R_{c1}}\right) \\ &=-\frac{\mu_0 l I_1}{4\pi R_{c1}}\left[\frac{(N_1-1)I_1}{N_1}+2I_2\theta(R_1-R_2)\right], \\ m_2\ddot{R}_{c2}&=\frac{\mu_0 l}{4\pi}I^2\frac{\partial}{\partial R_{c2}}L \\ &=\frac{\mu_0 l}{4\pi}\left(I_2^2\frac{\partial\hat{L}_{22}}{\partial R_{c2}}+2I_1I_2\frac{\partial\hat{L}_{12}}{\partial R_{c2}}\right) \\ &=-\frac{\mu_0 l I_2}{4\pi R_{c2}}\left[\frac{(N_2-1)I_2}{N_2}+2I_1\theta(R_2-R_1)\right], \end{aligned} \quad \text{(C5)}$$

where $\theta(z)$ is the Heaviside step function. Equations (C5) demonstrate that the inner array is imploded by its own current, whereas the outer array is additionally pushed to the axis by the interaction of its current with the azimuthal magnetic field generated by the current in the inner array.

APPENDIX D: FOURIER REPRESENTATION OF THE OPERATOR $\hat{H}$

The function $X(z_0,t)$, which is analytic in the unit circle, is thereby equal to the sum of its Taylor series

$$X(z_0,t)=\sum_{k=0}^{\infty}c_k(t)z_0^k, \quad \text{(D1)}$$

where $|z_0|\leqslant 1$ and the coefficients c_k are given by

$$c_k(t)=\frac{1}{2\pi i}\oint\frac{X(z_0,t)}{z_0^{k+1}}dz_0, \quad \text{(D2)}$$

where the integration contour is within the unit circle. At the boundary of the unit circle, Eqs. (14), (15), (D1) and (D2) yield

$$\begin{aligned} X(z_0,t)\big|_{z_0=\exp(iu)}&=\Psi(u,t)+i\Theta(\xi(u,t),t) \\ &=\sum_{k=0}^{\infty}c_k(t)e^{iku}, \\ c_k(t)&=\frac{1}{2\pi}\int_0^{2\pi}[\Psi(w,t)+i\Theta(\xi(w,t),t)]e^{-ikw}dw. \end{aligned} \quad \text{(D3)}$$

Separating the real and imaginary parts of Eq. (D3) and taking into account the Fourier expansion

$$\Psi(u,t)=\sum_{k=0}^{\infty}[a_k(t)\cos ku+b_k(t)\sin ku], \quad \text{(D4)}$$

where

$$\begin{aligned} a_k(t)&=\frac{1}{\pi}\int_0^{2\pi}\Psi(w,t)\cos(kw)dw, \\ b_k(t)&=\frac{1}{\pi}\int_0^{2\pi}\Psi(w,t)\sin(kw)dw, \end{aligned} \quad \text{(D5)}$$

one can obtain the following definition of the integral operator $\hat{H}$:

$$\begin{aligned} \hat{H}\Psi(u,t)&=\sum_{k=0}^{\infty}[a_k(t)\sin ku-b_k(t)\cos ku] \\ &=\frac{1}{\pi}\int_0^{2\pi}\Psi(w,t)\left[\sum_{k=1}^{\infty}\sin k(u-w)\right]dw \end{aligned} \quad \text{(D6)}$$

is equivalent to its original definition (6). Indeed,

$$\begin{aligned} \hat{H}\Psi(u,t)&=\frac{1}{\pi}\int_0^{2\pi}\Psi(w,t)\mathrm{Im}\left[\sum_{k=1}^{\infty}e^{ik(u-w)}\right]dw \\ &=\frac{1}{\pi}\int_0^{2\pi}\Psi(w,t)\mathrm{Im}\left[\frac{e^{i(u-w)}}{1-e^{i(u-w)}}\right]dw \\ &=\frac{1}{2\pi}\int_0^{2\pi}\Psi(w,t)\cot\left(\frac{u-w}{2}\right)dw. \end{aligned} \quad \text{(D7)}$$

Comparing Eqs. (D4) and (D6), we see that the operator $\hat{H}$ applied to a Fourier-series expansion of a real-valued function, changes the basis of the Fourier representation as follows: $\hat{H}(\cos ku,\sin ku)=(\sin ku,-\cos ku)$.

[1] C. Deeney, M. R. Douglas, R. B. Spielman, T. J. Nash, D. L. Peterson, P. L'Eplattenier, G. A. Chandler, J. F. Seaman, and K. W. Struve, Phys. Rev. Lett. **81**, 4883 (1998).

[2] C. Deeney, C. A. Coverdale, M. R. Douglas, T. J. Nash, R. B. Spielman, K. W. Struve, K. G. Whitney, J. W. Thornhill, J. P. Apruzese, R. W. Clark, J. Davis, F. N. Beg, and J. Ruiz-Camacho, Phys. Plasmas **61**, 2081 (1999).

[3] H. Sze, J. Banister, P. L. Coleman, B. H. Failor, A. Fisher, J. S. Levine, Y. Song, E. M. Waisman, J. P. Apruzese, R. W. Clark, J. Davis, D. Mosher, J. W. Thornhill, A. L. Velikovich, B. V. Weber, C. A. Coverdale, C. Deeney, T. Gilliland, J. McGurn, R. Spielman, K. Struve, W. Stygar, and D. Bell, Phys. Plasmas **8**, 3135 (2001).

[4] Y. Song, P. Coleman, B. H. Failor, A. Fisher, R. Ingermanson, J. S. Levine, H. Sze, E. Waisman, R. J. Commisso, T. Cochran, J. Davis, B. Moosman, A. L. Velikovich, B. V. Weber, D. Bell, and R. Schneider, Rev. Sci. Instrum. **71**, 3080 (2000).

[5] F. L. Cochran, J. Davis, and A. L. Velikovich, Phys. Plasmas **2**, 2765 (1995).

[6] A. L. Velikovich, F. L. Cochran, and J. Davis, Phys. Rev. Lett. **77**, 853 (1996); A. L. Velikovich, F. L. Cochran, J. Davis, and Y. K. Chong, Phys. Plasmas **5**, 3377 (1998).

[7] T. W. L. Sanford, R. C. Mock, R. B. Spielman, D. L. Peterson, D. Mosher, and N. F. Roderick, Phys. Plasmas **5**, 3737 (1998).

[8] J. Davis, N. A. Gondarenko, and A. L. Velikovich, Appl. Phys. Lett. **70**, 170 (1997).

[9] R. E. Terry, J. Davis, C. Deeney, and A. L. Velikovich, Phys. Rev. Lett. **83**, 4305 (1999).

[10] J. P. Chittenden, S. V. Lebedev, A. R. Bell, R. Aliaga-Rossel, S. N. Bland, and M. G. Haines, Phys. Rev. Lett. **83**, 100 (1999); J. P. Chittenden, S. V. Lebedev, S. N. Bland, F. N. Beg, and M. G. Haines, Phys. Plasmas **8**, 2305 (2001).

[11]D. L. Peterson, R. L. Bowers, K. D. McLenithan, C. Deeney, G. A. Chandler, R. B. Spielman, M. K. Matzen, and N. F. Roderick, Phys. Plasmas **5**, 3302 (1998).
[12]D. L. Peterson, R. L. Bowers, W. Matuska, K. D. McLenithan, G. A. Chandler, C. Deeney, M. S. Derzon, M. Douglas, M. K. Matzen, T. J. Nash, R. B. Spielman, K. W. Struve, W. A. Stygar, and N. F. Roderick, Phys. Plasmas **6**, 2178 (1999).
[13]L. I. Rudakov, A. L. Velikovich, J. Davis, J. W. Thornhill, J. L. Giuliani, Jr., and C. Deeney, Phys. Rev. Lett. **84**, 3326 (2000); A. L. Velikovich, L. I. Rudakov, J. Davis, J. W. Thornhill, J. L. Giuliani, Jr., and C. Deeney, Phys. Plasmas **7**, 3265 (2000).
[14]S. V. Lebedev, F. N. Beg, S. N. Bland, J. P. Chittenden, A. F. Dangor, M. G. Haines, K. H. Kwek, S. A. Pikuz, and T. A. Shelkovenko, Phys. Plasmas **8**, 3734 (2001).
[15]S. V. Lebedev, F. N. Beg, S. N. Bland, J. P. Chittenden, A. F. Dangor, M. G. Haines, K. H. Kwek, S. A. Pikuz, and T. A. Shelkovenko, Phys. Rev. Lett. **85**, 98 (2000).
[16]S. V. Lebedev, R. Aliaga-Rossel, S. N. Bland, J. P. Chittenden, A. E. Dangor, M. G. Haines, and M. Zakaullah, Phys. Rev. Lett. **84**, 1708 (2000); J. P. Chittenden, S. V. Lebedev, S. N. Bland, A. Ciardi, and M. G. Haines, Phys. Plasmas **8**, 675 (2001).
[17]R. B. Baksht, A. Y. Labetsky, S. V. Loginov, V. I. Oreshkin, A. V. Fedyunin, and A. V.Shishlov, Plasma Phys. Rep. **23**, 119 (1995); R. B. Baksht, A. Y. Labetsky, A. G. Rousskikh, A. V. Fedyunin, A. V. Shishlov, V. A. Kokshenev, and N. E. Kurmaev, *ibid.* **27**, 557 (2001).
[18]E. M. Waisman, J. Appl. Phys. **50**, 23 (1979).
[19]A. I. Dyachenko, V. E. Zakharov, and E. A. Kuznetsov, Plasma Phys. Rep. **22**, 829 (1996).
[20]M. A. Lavrentyev and B. V. Shabat, *Problems of Hydrodynamics and Their Mathematical Models*, 2nd ed. (in Russian) (Nauka, Moscow, 1977); Z. Nehari, *Conformal Mapping* (McGraw Hill, New York, 1952).
[21]I. E. Parshukov, Ph. D. thesis (in Russian), Chelyabinsk State University, Chelyabinsk, Russia, 1997.
[22]L. D. Landau and E. M. Lifshitz, *Electrodynamics of Continuous Media* (Pergamon, New York, 1984).
[23]A. Russell, J. Inst. Electr. Eng. **62**, 1 (1923); **69**, 270 (1931); F. W. Grover, *Inductance Calculations/Working Formulas and Tables* (Van Nostrand, New York, 1946), p. 43.
[24]J. Katzenstein, J. Appl. Phys. **52**, 676 (1981).
[25]N. A. Bobrova, T. L. Razinkova, and P. V. Sasorov, Sov. J. Plasma Phys. **14**, 617 (1988); **18**, 269 (1992); in *Dense Z-Pinches*, 3rd International Conference, AIP Conf. Proc. 299, London, United Kingdom, 19–23 April 1993, edited by M. Haines and A. Knight (American Institute of Physics, New York, 1994), p. 10.
[26]R. Menikoff and C. Zemach, J. Comput. Phys. **51**, 28 (1983); G. Hazak, Phys. Rev. Lett. **76**, 4167 (1996); A. L. Velikovich and G. Dimonte, *ibid.* **76**, 3112 (1996); N. J. Zabusky, Annu. Rev. Fluid Mech. **31**, 495 (1999).